Disordered stoichiometric nanorods and ordered off-stoichiometric nanoparticles in n-type thermoelectric $Bi_2Te_{2.7}Se_{0.3}$

AIP | Journal of Applied Physics

Disordered stoichiometric nanorods and ordered off-stoichiometric nanoparticles in n-type thermoelectric Bi2Te2.7Se0.3

Chris E. Carlton, Chris A. Kuryak, Wei-shu Liu, Zhifeng Ren, Gang Chen et al.

Citation: J. Appl. Phys. **112**, 093518 (2012); doi: 10.1063/1.4759285
View online: http://dx.doi.org/10.1063/1.4759285
View Table of Contents: http://jap.aip.org/resource/1/JAPIAU/v112/i9
Published by the American Institute of Physics.

Disordered stoichiometric nanorods and ordered off-stoichiometric nanoparticles in n-type thermoelectric $Bi_2Te_{2.7}Se_{0.3}$

Chris E. Carlton,[1,a)] Chris A. Kuryak,[1] Wei-shu Liu,[2] Zhifeng Ren,[2] Gang Chen,[1] and Yang Shao-Horn[1,a)]
[1]*Department of Mechanical Engineering, Massachusetts Institute of Technology, Cambridge, Massachusetts 02139, USA*
[2]*Department of Physics, Boston College, Chestnut Hill, Massachusetts 02467, USA*

(Received 5 July 2012; accepted 25 September 2012; published online 8 November 2012)

N-type $Bi_2Te_{2.7}Se_{0.3}$ bulk thermoelectric materials with peak *ZT* values up to ~1 were examined by transmission electron microscopy and electron diffraction. Two nanostructural features were found: (i) a structural modulation of ~10 nm, which consisted of nanorods with crystalline and nearly amorphous regions, having the rod axes normal to (0,1,5)-type planes, and wave vector normal to (1,0,10)-type planes and (ii) non-stoichiometric ordered Bi-rich nanoparticles. The presence of the structural modulation was not influenced by the ion milling energy or temperature in this study while the non-stoichiometric ordered nanoparticles were only observed when ion milling at low temperatures and low energy was used. It is proposed that both the structural modulation of ~10 nm and the presence of non-stoichiometric nanoparticles are responsible for the low lattice thermal conductivity (~0.6 W/mK) of the $Bi_2Te_{2.7}Se_{0.3}$ bulk thermoelectric materials studied. © *2012 American Institute of Physics*. [http://dx.doi.org/10.1063/1.4759285]

I. INTRODUCTION

Recent efforts have been focused on developing thermoelectric materials for clean energy production and waste heat recovery technology.[1] Thermoelectric generators convert temperature gradients directly into electrical energy without use of moving parts,[1] which makes them attractive for applications that transform low-grade heat into useful energy; namely solar thermal power[2] and automotive waste heat reclamation.[3] However, the efficiencies of these technologies are limited by the performance of thermoelectric materials. The ideal efficiency of a thermoelectric junction, η, can be given by[1]

$$\eta = \frac{\sqrt{1+ZT}-1}{\sqrt{1+ZT}+\frac{T_C}{T_H}}, \quad (1)$$

where T_C and T_H are the temperatures of the cold and hot junctions, respectively. *ZT* is the dimensionless figure of merit, which is governed by the physical properties of thermoelectric materials as given by

$$ZT = \frac{\sigma S^2 T}{\kappa}, \quad (2)$$

where σ is the electrical conductivity, *S* is the Seebeck coefficient, *T* is the mean temperature, and κ is the total thermal conductivity (including both lattice and electronic thermal conductivity). Thermoelectric materials based on Bi_2Te_3 and the solid solutions of Bi_2Se_3 and Sb_2Se_3 are known to achieve high *ZT* values near room temperature,[4] where p-type $Bi_{2-x}Sb_xTe_3$ and n-type $Bi_2Te_{2-x}Se_x$ bulk materials can achieve *ZT* values of ~1.1 and ~0.85,[5,6] respectively. This is because they have high electrical conductivities (~1000 S/cm),[7,8] low lattice thermal conductivities (~1.2 W/mK),[9–11] and high Seebeck coefficients (~±200 μV/K).[7,8] Introducing nanostructures[12] in thermoelectric materials has been shown to reduce thermal conductivity and thus increase *ZT* because nanostructures scatter phonons more effectively than electrons as phonons have a long mean free path compared to electrons. Markedly enhanced *ZT* values have been reported in 6 nm superlattices of Bi_2Te_3/Sb_2Te_3,[13] which have been attributed to decreased lattice thermal conductivity. More recently, nanostructured p-type $Bi_{2-x}Sb_xTe_3$ bulk alloys have shown decreased lattice thermal conductivity and enhanced *ZT*.[14]

Interestingly, Bi_2Te_3-based bulk materials[9,10,15–20] and superlattices[9] are known to exhibit naturally nanoscale structural modulations, which could contribute to the low lattice thermal conductivity ($\kappa_{lattice}$) of these materials. In particular, the work of Peranio *et al.*[9,10,15,21] has shown that the nanoscale structural modulation has a wavelength of ~10 nm and a wave vector parallel to $g_{\{1,0,10\}}$, which is related to a sinusoidally varying strain domain structure with no detectable compositional difference.[15] In this paper, we are interested in understanding whether natural modulations are also present in recently reported nanostructured n-type $Bi_2Te_{2.7}Se_{0.3}$ bulk materials.[8]

Here, we study recently reported n-type $Bi_2Te_{2.7}Se_{0.3}$ samples (with ZT values up to ~1) that were synthesized by mechanical alloying and hot pressing,[8] where as-pressed and re-pressed samples show very low thermal conductivities having $\kappa_{lattice}$ about 0.6 W/mK. Some differences in the transport properties between as-pressed and re-pressed samples along and perpendicular to the hot-press direction are noted (Fig. S1),[33] which has been attributed to different degrees of texture (having the a-b plane oriented

a)Authors to whom correspondence should be addressed. Electronic addresses: carltonc@mit.edu and shaohorn@mit.edu.

perpendicular to the press direction) and intrinsic anisotropy in the transport properties.[23] The Bi_2Te_3 crystal structure consists of five-layer-units of Te-Bi-Te-Bi-Te stacked along the c axis, which form pseudo-NaCl lamellae having a thickness of ~1 nm, as shown in Fig. 1. The lamellae are held together with covalent bonds and van der Waals bonds along the c axis (Fig. 1), which are responsible for anisotropy in transport properties.[23] In this report, we study the as-pressed and repressed samples using TEM along orientations both perpendicular and parallel to the press direction to examine if there are any differences in the nanoscale features. As recent work of Medlin *et al.*[24] has suggested that the presence of structural modulation might be influenced by the conditions of ion milling, we compare TEM samples prepared using the low energy and low temperature (LELT) ion milling procedure of Medlin *et al.*[24] and samples prepared by the conventional high energy room temperature (HERT) methods used in previous work.[9,10]

II. RESULTS AND DISCUSSION

A. Nanorods

Representative bright-field and dark-field images of repressed $Bi_2Te_{2.7}Se_{0.3}$ are shown in Fig. 2 and representative as-pressed and re-pressed images are compared in Fig. S2, all of which reveal a nanoscale structural modulation with a period of ~10 nm consisting of light and dark fringes of ~5 nm (Fig. 1(b)) and a wave vector parallel to the $(0,\bar{1},10)$ plane normal similar to those reported previously.[9,10,15–18] The nanoscale structural modulation was found present in one direction shown in Figs. 2(a)–2(c), and in multiple directions shown in Fig. 2(d) and Figs. 2(a) and 2(b). These fringes were oriented normal to the (0,1,5)-type planes, and in cases where (0,1,5)-type reflections were not in the diffraction patterns, stereographic projections were used to locate them in three dimensional space and project them onto perspective zone axes (Fig. S3). There are three (0,1,5)-type planes in the structure of Bi_2Te_3 with space group of $R\bar{3}m$ defined in a hexagonal unit cell ($\boldsymbol{a} = 4.495$ Å and $\boldsymbol{c} = 30.440$ Å), which are nearly orthogonal. Therefore, the nanoscale structural modulation forms a nearly cubic three-dimensional lattice (Fig. S4), which supports previous work.[10]

The structural modulation was observed in all grains in both as-pressed and re-pressed samples (typical grains were larger than 1 μm). It should be mentioned that unlike previous work,[9,10,18,24] the presence of the structural modulation was not influenced by the ion milling conditions used in the TEM preparation because samples prepared by LELT and HERT ion milling were found to exhibit the structural modulation. In addition, the structural modulation was found in as-pressed $Bi_2Te_{2.7}Se_{0.3}$ that was prepared by crushing the bulk material in a mortar and pestle, which confirms that the structural modulation is not an artifact of ion milling. Moreover, similar structural modulation was noted in single crystal $Bi_2Te_{2.99}$ TEM samples that were prepared by scraping the bulk material with a razor blade (Fig. S5). It should be noted that the structural modulation observed is markedly different from dislocations found in these samples, few dislocations were visible, and there were only visible when the structural modulation was out of contrast.

Using electron diffraction data collected from low symmetry zone axes (LSZAs) and high resolution TEM (HRTEM), we propose that the structural modulation results from an assembly of ~5 nm thick nanorods with alternating high and low crystallinity, and the nanorods have rod axes normal to the (0,1,5)-type planes. Electron diffraction patterns from LSZAs revealed additional information compared to the diffraction patterns from the high symmetry zone axes (HSZAs) shown in previous work[9,10] and in Fig. 2. One representative pattern in Fig. 3 shows (i) diffuse streaks highlighted in Fig. 3(b), (ii) diffuse ring highlighted in Fig. 3(d), and (iii) reflections forbidden in the zone axis in Fig. 3(e). First, the diffuse streaks can be understood by considering the fact that crystalline nanorods in real space produce disks of diffuse contrast in reciprocal space,[25] and the intersection of the these disks with the Ewald sphere yields the diffuse streaks in Figs. 3(b) and 3(c). There are two nearly perpendicular sets of streaks noted in Fig. 3, which are normal to the (0,1,5) and $(\bar{1},0,5)$ planes. Even though (0,1,5) and $(\bar{1},0,5)$ do not appear in the zone axis, Fig. S6 shows that there are relatively small angles between these planes and

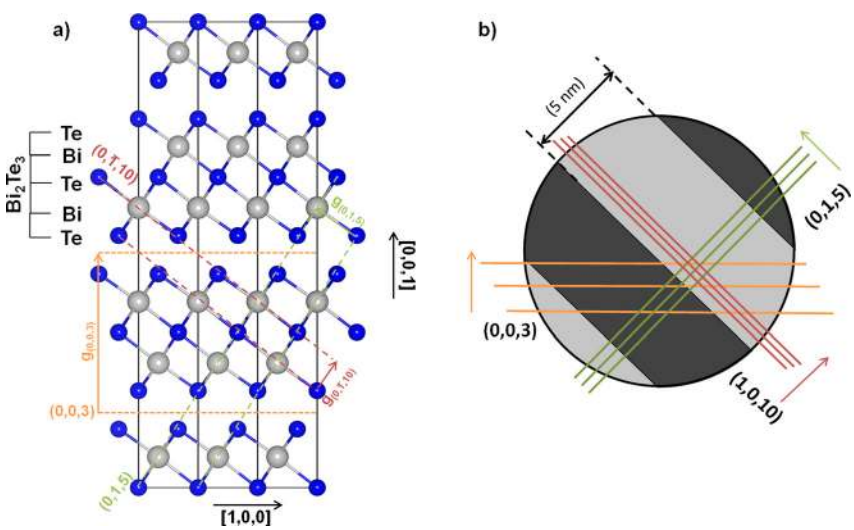

FIG. 1. (a) A model of the Bi_2Te_3 structure projected in the [1,0,0] direction, which was created using the VESTA software.[22] The gray atoms represent Bi and the blue atoms represent Te. The Bi_2Te_3 structure consists of five covalently bonded five layer lamellae with Te-Bi-Te-Bi-Te stacking with van der Waals bonding in between the lamellae. Bi_2Te_3 has space group of $R\bar{3}m$, which is defined typically in a hexagonal unit cell with lattice parameters $\boldsymbol{a} = 4.495$ Å and $\boldsymbol{c} = 30.440$ Å. (b) A schematic of the nanostructure found in Bi_2Te_3. The crystalline material (light gray area) is ~5 nm wide and is oriented normal to the (0,1,5) planes. There is an approximately 31° angle between (0,1,5) and (0,0,3) in the Bi_2Te_3 structure. In the R-3 m structure, the (0,1,5) plane is equivalent to the $(\bar{1},0,5)$ and $(1,\bar{1},5)$ planes.

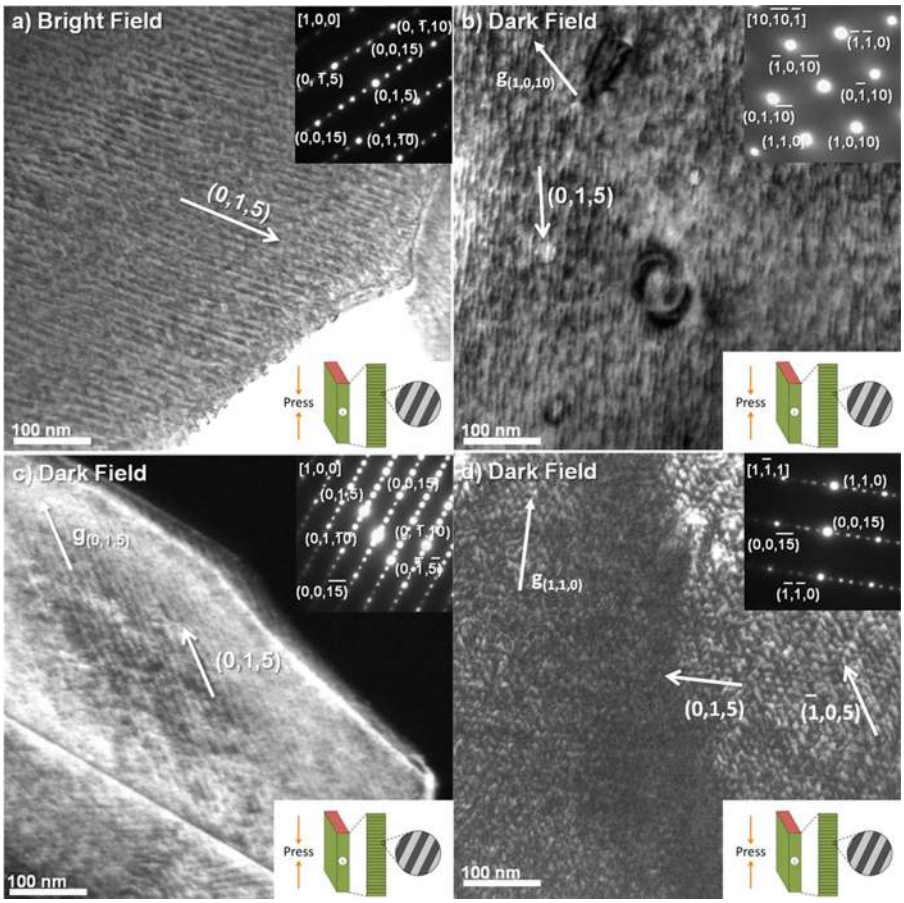

FIG. 2. Diffraction contrast images of nanoscale structural modulations in re-pressed $Bi_2Te_{2.7}Se_{0.3}$ that were taken with the beam perpendicular to the direction of pressing. (a) is in bright field, and (b)–(d) are in dark field, and the (0,1,5) plane normal is indicated. LELT ion milling was used for (b) and (c) while HERT ion milling was used for (a) and (d).

the zone axis. Therefore, the structural modulation consists of nanorods of ~5 nm with axes that are crystallographically aligned normal to the (0,1,5) and $(\bar{1},0,5)$ planes. Second, the diffuse ring in the diffraction pattern can be explained by the presence of nanorods with low crystallinity in the structural modulation as the structural modulation, along the $(1,\bar{1},5)$ plane normal, is closely parallel to the zone axis (Figure S6). Amorphous materials and/or materials with low crystallinity can produce diffuse rings in electron diffraction patterns (EDPs) because they have poorly defined atomic positions leading to a distribution of interatomic spacings that cause a diffuse ring.[25] Third, the presence of off-zone axis diffraction spots [Fig. 3(e)] is due to the very small reciprocal dimension along the c*-axis associated with the very large lattice parameter along the c-axis of the Bi_2Te_3 crystal structure, which allows the reciprocal lattice rods that are forbidden by the zone axis to penetrate the Ewald sphere and therefore appear in the electron diffraction pattern.

Previous TEM studies of Bi_2Te_3 based materials do not report diffuse streaks or diffuse rings in their EDPs.[9,10,16,19,20] One possible explanation for the difference is that the diffraction patterns with diffuse features in this study were obtained

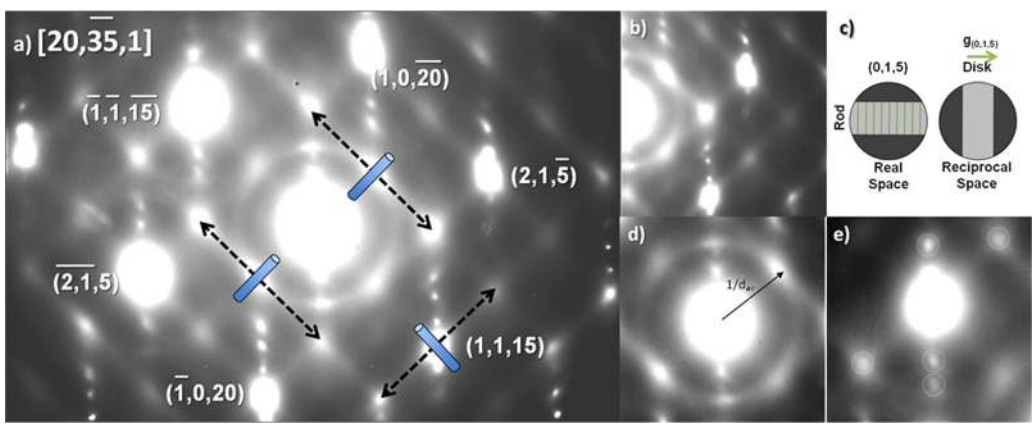

FIG. 3. The [20,35,1] EDP. (a) The indexed diffraction pattern, (b) the detail of the streaks in the EDP and (c) a scheme of how nanorods become disks of diffuse contrast in reciprocal space. The nanorod orientation is overlaid on (a) and the lines extending from the rods indicate the direction of streaking. (d) Detailed view of the central ring in EDP and (e) details on the closely spaced spots that appear in the EDP even though they are forbidden by the zone axis.

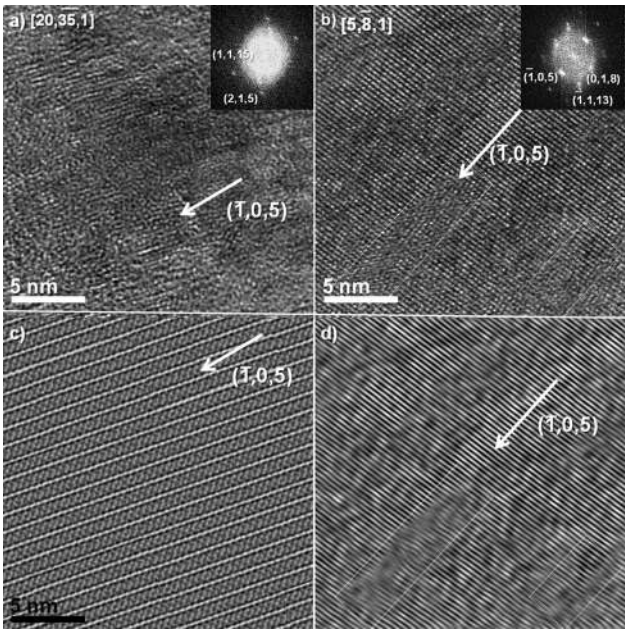

FIG. 4. (a) HRTEM imaging from the same crystal and zone axis as Fig. 3 shows that the region appears nearly amorphous. (c) HRTEM simulation of the [20,$\bar{3}$5,1] zone axis using the SIMULATEM software.[26] (b) HRTEM of a nearby zone axis in the same crystal, where the lattice fringes are clearly resolved. The arrow in (b) indicates an area where the contrast from the ($\bar{1}$,0,5) lattice fringes disappears, indicating low crystallinity. (d) Fourier filtering of the ($\bar{1}$,0,5) planes, which highlights the crystallographic disorder in these planes.

from LSZAs such as [20,$\bar{3}$5,1], which can have (i) lower densities of diffraction spots and (ii) lower intensity diffraction spots compared to HSZAs such as [1,0,0] and [5,$\bar{5}$,1] reported previously[9,10,16] to allow the observation of diffuse features that would otherwise be washed out in the HSZAs.

The presence of regions with low crystallinity was further supported by HRTEM of the crystal shown in Fig. 3 along the same zone axis, where no visible lattice fringes were observed in Fig. 4(a). Preliminary TEM simulation performed using the SIMULATEM software[26] revealed that the slightly out-of-plane (0,0,3) lattice fringes should appear for this zone axis [Fig. 4(b)], where a spherical aberration of 0.5 mm, the nominal spherical aberration of the JOEL 2010 F used in this work, was used and the simulation was performed at Scherzer defocus. It is interesting to note that continuous lattice fringes of ($\bar{1}$,0,5) were observed when the same crystal was tilted to a nearby zone axis, as shown in Fig. 4(b). White boxes in Fig. 4(b) indicate the regions, where the contrast on the ($\bar{1}$,0,5) lattice fringes is lost. Fourier filtered HRTEM (FFHRTEM) imaging on the $g_{(\bar{1},0,5)}$ lattice vector further supports the presence of nanorods of low crystallinity normal to the ($\bar{1}$,0,5) planes. Our interpretation of the HRTEM images in Fig. 4, which was aided by our understanding of electron diffraction data, is different from previous HRTEM studies of $Bi_2Te_{2.7}Se_{0.3}$ materials,[16,18] where terminating and wavy lattice planes in the FFHTREM

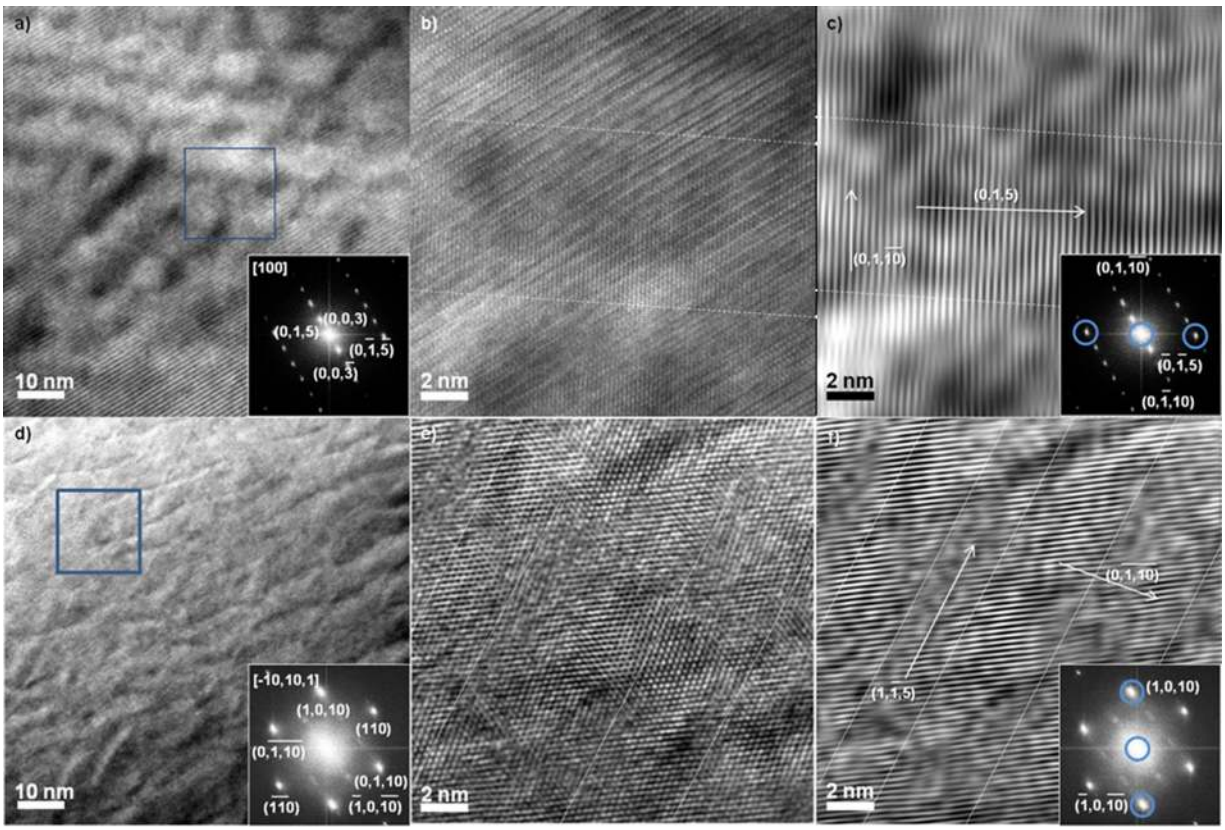

FIG. 5. (a) and (d) are zone-axis-aligned, low-magnification HRTEM images with inset FFTs of re-pressed $Bi_2Te_{2.7}Se_{0.3}$ that was prepared via LELT ion milling and clearly show the nanoscale structural modulation. (b) and (e) show increased magnifications of (a) and (d) respectively. (c) and (f) present FFHRTEM of (b) and (e) using $g_{(0,1,5)}$ and $g_{(1,0,10)}$ respectively. Alternating regions of high and low crystallinity are clearly seen in (c) and (f). Comparison of (c) and (f) with (a) and (d) demonstrates that the alternating light/dark contrast of the low magnification images is associated with the alternating high and low crystallinity of the Fourier filtered images.

was used as evidence of dislocations,[18] phase disorder in the basal planes,[16] or a sinusoidal displacement field.[9,10,15,19,21]

In order to confirm that the bright and dark oscillations in the diffraction contrast images were correlated with nanorods of high and low crystallinity, series of HRTEM images at different magnifications were made from the same areas (Fig. 5). This allowed direct comparison of the nanoscale structural modulation and atomic-scale structural features and clearly shows that the bright regions in the HRTEM images are directly associated with low crystallinity. HRTEM images along the [1,0,0] and [$\bar{1}$0,10,1] zone axes are shown in Figs. 5(a)–5(f), respectively, where 2 sets of structural modulation are visible. Boxed regions in Fig. 5(a) and 5(d) are imaged at a higher magnification in Figs. 5(b) and 5(e), respectively. FFHRTEM imaging on the $g_{(0,1,5)}$-type lattice vectors (Fig. 5(c)) revealed nanorods of low crystallinity in the (0,1,5)-type planes, analogous to the findings of $(Bi_{0.25}Te_{0.75})_2Te_3$ by Jacquot *et al.*,[19] while FFHRTEM imaging of the $g_{(1,0,10)}$-type lattice vectors (Fig. 5(f)) shows similar disorder, indicating that the natural nanostructure also distorts non-(0,1,5)-type planes. It should be noted that the light and dark regions have comparable chemical compositions as revealed from energy dispersive spectroscopy in the TEM (Fig. S7), therefore the observed modulation contrast is not induced by large differences in the chemical composition.

We show that all grains of as-pressed and re-pressed $Bi_2Te_{2.7}Se_{0.3}$ samples exhibit a nanoscale structural modulation, which consists of alternating nanorods of ~5 nm with high and low crystallinity with rod axes normal to the (0,1,5)-type planes when viewed both along the press direction and perpendicular to the press direction. Our findings, combined with previous work,[9,10,16–20] indicate that the nanoscale structural modulation found in $Bi_{2-x}Sb_xTe_{3-y}Se_y$ materials might be a general feature that is responsible for their low lattice thermal conductivity by effectively scattering phonons (schematically illustrated in Fig. S8). Further studies are needed to understand the physical origin of the structural modulation and how processing may influence the structural modulation, which may lead to the development of strategies to significantly improve ZT by tuning the structural modulation.

B. Ordered off-stoichiometric Bi-rich nanoparticles

Bright-field TEM imaging of the as-pressed [Figs. 6(a) and 6(b)] and re-pressed samples [Figs. 6(c) and 6(d)] revealed the presence of nanoparticles of 10–100 nm in the matrix of large grains when prepared via LELT ion milling, where the as-pressed sample appeared to have more nanoparticles than the re-pressed sample. Detailed analysis of ten TEM images for each sample showed that the as-pressed samples contained smaller nanoparticles of ~25 nm than the re-pressed samples of ~34 nm, as shown in Figs. 6(c) and 6(f), respectively. In addition, the percentage of the projected area of the TEM images occupied by nanoparticles was analyzed, giving values of 4.3% and 2.5% in the as-pressed and re-pressed samples, respectively (Fig. S9). As the nanoparticles

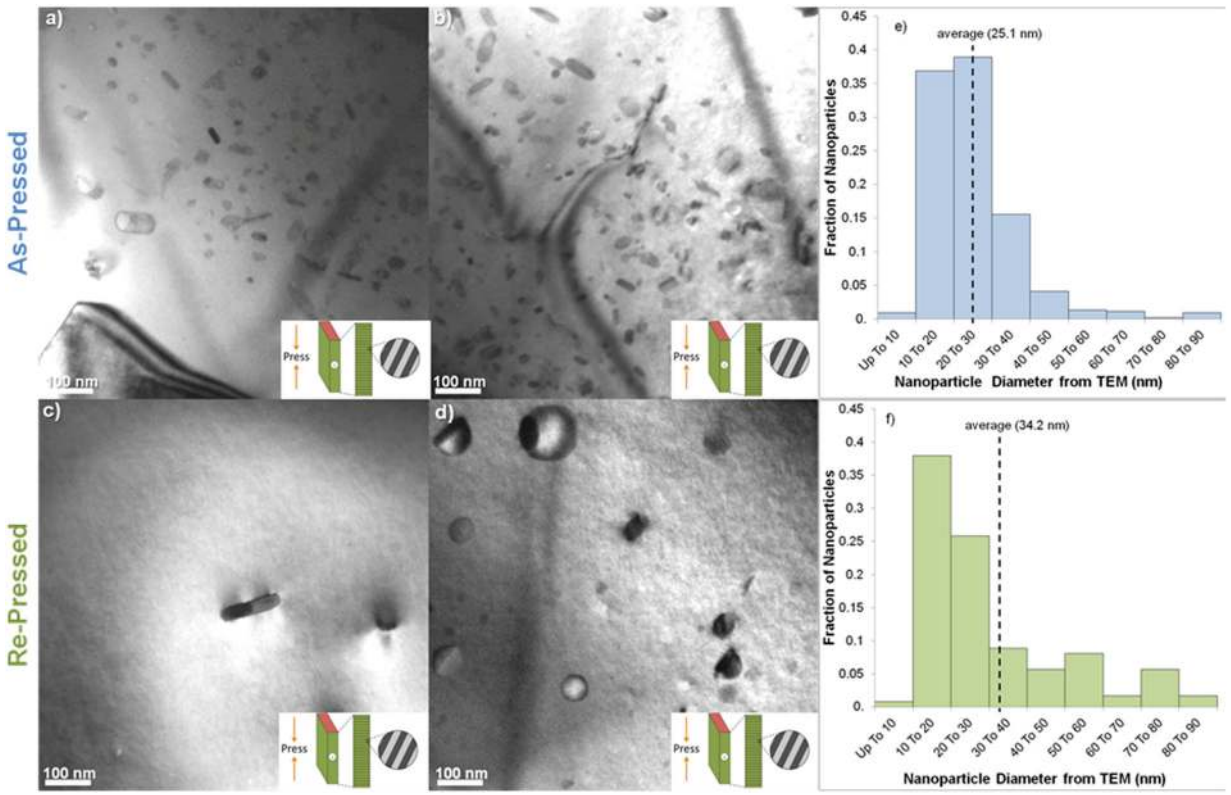

FIG. 6. Bright-field TEM of LELT ion-milled $Bi_2Te_{2.7}Se_{0.3}$ samples. Each image shows one grain containing several nanoparticles (dark spots). (a) and (b) The as-pressed sample shows a high number density of nanoparticles, whereas the (c) and (d) re-pressed sample contains a low number density of nanoparticles. All images are perpendicular to the press direction. (e) The histogram of nanoparticle diameters reveals that the re-pressed sample contained larger particles than the as-pressed sample, on average.

appear to have a disk shape, which is evident from observed circle and oval particles in the TEM images (Fig. 6), we can set the area fraction as the upper limit for the volume fraction of these particles because the TEM sample cross-section thickness ($<\sim$200 nm) is equal to or greater than the nanoparticle thickness.

HRTEM imaging in conjunction with EDS analysis was used to show that these nanoparticles are off-stoichiometric relative to the nominal composition of $Bi_2Te_{2.7}Se_{0.3}$ or "Bi_2Te_3." The EDS results showed that most nanoparticles were found to be Bi-rich (Table S1), where the concentration of Se was too low to quantify. Typical HRTEM images of nanoparticles show interplanar spacings greater than 1 nm. A HRTEM image collected from the as-pressed sample shows the lattice fringes of a nanoparticle near the [1,0,0] zone axis, which reveals an interplanar spacing of 1.4 nm (Fig. 7) larger than that the largest spacing of 1.0 nm expected for the Bi_2Te_3 structure with space group $R\bar{3}m$[Fig. 7(b)]. The difference in the lattice fringes shown in Figs. 7(a) and 7(b) can be explained by the infinite adaptability[27,28] of the Bi_2Te_3 structure, which can be thought as a modulated Bi-Te (NaCl) structure[27,28] that can accommodate different stoichiometries by either (i) inserting Bi_2 bilayers into the pseudo-NaCl blocks[28] or (ii) changing the number of layers in the pseudo-NaCl blocks through the addition or subtraction of -Bi-Te bilayers.[27] The larger lattice fringe spacing of the nanoparticle in Fig. 7 can be explained by introducing an extra bilayer of Bi into the unit cell of Bi_2Te_3, where the normal Te-Bi-Te-Bi-Te stacking and the Bi_2Te_3 composition are changed to the Te-Bi-Te-Bi-Te-Bi-Bi stacking and Bi_4Te_3

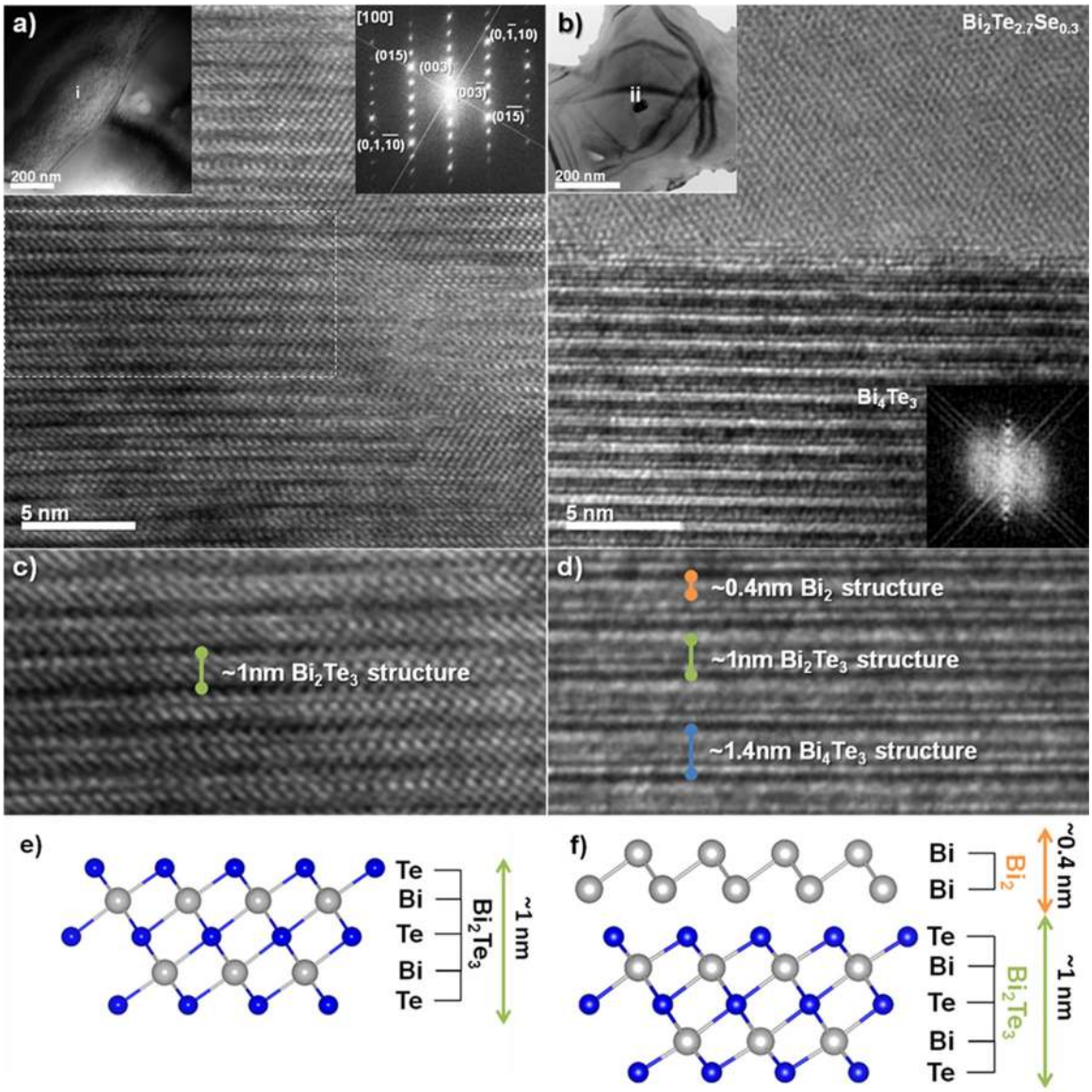

FIG. 7. (a) HRTEM of re-pressed $Bi_2Te_{2.7}Se_{0.3}$ prepared by LELT ion milling. The FFT of (a) in right inset was indexed to the Bi_2Te_3 structure in the zone axis of [1,0,0]. The HRTEM was taken in the grain marked (i) and (c) is a magnified image of the boxed region in (a). (b) HRTEM of a nanoparticle in as-pressed $Bi_2Te_{2.7}Se_{0.3}$ that was ion milled at LELT. The nanoparticle is on bottom half of the image, and the FFT of the nanoparticle indicates a lattice spacing of 1.4 nm. (d) Magnified HRTEM from the nanoparticle in (b). (e) A scheme of the Bi_2Te_3 structure, which consists of five-layer covalently bonded Te-Bi-Te-Bi-Te stacks with van der Waals bonds between the outer Te layers. (f) A scheme of the Bi_4Te_3 structure, which consists of a Bi_2 layer and a Bi_2Te_3 layer combining to make the repeating Bi_4Te_3 lamella.

composition, respectively. This hypothesis is supported by the fact that the HRTEM image in Fig. 7(b) is similar to that of bulk Bi_4Te_3 reported previously by Ciobanu *et al.*[28] All of the nanoparticles studied by HRTEM in this work were Bi-rich and had interplanar spacings along the c-axis that were greater than 1.0 nm, but they were not necessarily Bi_4Te_3. The presence of these nonstoichiometric nanoparticles might be a result of the synthesis route used. As the samples used in this study were synthesized by the mechanical alloying of elemental powders followed by hot-pressing,[8] it is very likely that these nonstoichiometric nanoparticles can result from inhomogeneous mixing of the elements. This hypothesis is further supported as the reduction in nanoparticle density upon repressing.

Ordered Bi-rich off-stoichiometric nanoparticles are reported, for the first time, in $Bi_2Te_{2.7}Se_{0.3}$-based thermoelectric materials. As nanograins,[29,30] nanoparticles,[14,20] and nanovoids[20,31] in Bi_2Te_3-based materials have been correlated with reductions in $\kappa_{lattice}$, it is proposed that these nanoparticles could have a significant effect in lowering the $\kappa_{lattice}$ of $Bi_2Te_{2.7}Se_{0.3}$ showing $\kappa_{lattice} \sim 2\times$ lower than single crystal samples.[8–10] This hypothesis is supported by recent theoretical work that has shown that even low volume percentages (1%-5%) of nanoparticles with diameters between 10 and 100 nm can lead to substantial reduction ($\sim$2-4$\times$) in $\kappa_{lattice}$ for SiGe.[32] The control and optimization of the nonstoichiometric nanoparticles could provide an effective way to lower the thermal conductivity of $Bi_{2-x}Sb_xTe_{3-y}Se_y$ materials.

We found that these nonstoichiometric nanoparticles (Fig. 6) were not present in the samples prepared by HERT ion milling. It is likely that the nanoparticles were preferentially milled away at HERT conditions, leaving voids in the material. The hypothesis is supported by the observation of voids in samples milled by with HERT settings (Fig. S10). As most of previous TEM investigations of Bi_2Te_3-based materials have used HERT ion milling,[9,10,18] it is possible that nonstoichiometric nanoparticles are a common feature in Bi_2Te_3-based materials but they are not observed because they could have been removed during TEM sample preparation. This highlights the importance of establishing a standard TEM sample preparation technique for future TEM investigation of Bi_2Te_3-based materials that is delicate enough to minimize artifacts.

III. CONCLUSIONS

Our TEM studies of high-*ZT* $Bi_2Te_{2.7}Se_{0.3}$ bulk samples show the presence of (i) nanoscale structural modulation having alternating nanorods with high and low crystallinity extending throughout all grains, which have rod axes normal to the (0,1,5)-type planes and (ii) ordered nonstoichiometric Bi-rich nanoparticles. It is proposed that the presence of nanorods with low crystallinity is a general feature of Bi_2Te_3-based materials because similar structural modulation has been reported by previous studies in a wide variety of sample compositions and sample geometries, including thin films,[9] single crystals [Fig. S5(b)] in this study and bulk polycrystals (Fig. 2) in this study and previous work.[9,10,16] It is proposed that both nanorods with low crystallinity and ordered non-stoichiometric nanoparticles contribute to phonon scattering and largely responsible for the low $\kappa_{lattice}$ of the samples studied. Further investigations into control of these nanostructures could potentially be very fruitful for the continued enhancement of *ZT* and the efficiency of thermoelectric power generation.

IV. EXPERIMENTAL METHODS AND MATERIALS

As-pressed and re-pressed thermoelectric samples were prepared by mechanical alloying and hot-pressing and characterized by techniques identical to those outlined in Yan *et al.*[8] X-ray diffraction data of these samples are presented in Fig. S11. TEM samples were mechanically polished and thinned by a successive series of diamond lapping films until both sides were flaw free and the sample thickness was below 100 μm. The polished samples were then ion milled under 4 eV at room temperature using a Fischione 1010 or a Gatan PIPS, and these samples were referred to as HERT. To investigate the effect of ion beam damage, some samples were milled at low temperature and accelerating voltage following the procedure outlined by Medlin *et al.*[24] using only the Fischione 1010. The LELT ion milling in this work was done using a Fischione 1010 ion mill at $-100\,^{\circ}$C and involved three steps, (1) milling at 10°, 4.5 KeV, and 5 mA until perforation, (2) milling at 8°, 3.0 KeV, and 5 mA to enlarge the hole, and (3) milling at 6°, 1 KeV, and 3 mA to polish the sample and remove any remaining damage.

The TEM analysis was performed on a JEOL 2010F TEM equipped with a Schottky emission gun. Bright field diffraction contrast images were collected by centering the smallest objective aperture (20 μm) on the transmitted beam. Dark field diffraction contrast images were created by using the beam tilt controls to align a diffracted beam with the optic axis, and then centering the smallest objective aperture on it. The diffraction contrast TEM was performed in the many beam condition at the zone axes. Zone axes were located by tilting the sample along Kikuchi lines produced by convergent beam electron diffraction. Processing of the TEM images was performed using Gatan Digital Micrograph software. For the FFHRTEM, an FFT was made from the HRTEM image. The FFT spots associated with a single $g_{(h,k,l)}$ and the non-periodic information associated with g_0 were then selected and all other periodic data were removed and an inverse FFT was performed. Non-periodic information from near the $g_{(0,0,0)}$ spot was included to improve the view-ability of the FFHRTEM image. The conventional EDS data were collected and quantified with the INCA software. The M-series was used for Bi quantification and L-series was used for Te and Se. The aberration corrected STEM EDS mapping was conducted at the Oak Ridge National Laboratory's High Temperature Materials Laboratory on a JEOL 2200F equipped with a pre-objective aberration corrector manufactured by CEOS.

ACKNOWLEDGMENTS

This work was supported as part of the Solar-Thermal Energy Conversion Center (S3TEC), an Energy Frontier

Research Center funded by the U.S. Department of Energy, Office of Science, Office of Basic Energy Sciences under Award No. DE-FG02-09ER46577. The EDS mapping was performed with the assistance of Dr. Lawrence Allard at the Oak Ridge National Laboratory's High Temperature Materials Laboratory was sponsored by the U.S. Department of Energy, Office of Energy Efficiency and Renewable Energy, Vehicle Technologies Program. The authors would like to thank Y. S. Lee and D. Gardner (MIT) for providing the single crystal samples as well as Dr. Shuo Chen (Boston College) for her contributions to this work.

[1]D. Rowe, in *Thermoelectrics Handbook*, edited by D. Rowe (CRC, 2005), p. 1.
[2]D. Kraemer, B. Poudel, H.-P. Feng, J. C. Caylor, B. Yu, X. Yan, Y. Ma, X. Wang, D. Wang, A. Muto, K. McEnaney, M. Chiesa, Z. Ren, and G. Chen, Nature Mater. **10**(7), 532 (2011).
[3]J. Yang, presented at the 24th International Conference on Thermoelectrics, (Clemson, South Carolina, 2005).
[4]A. Majumdar, Science **303**(5659), 777 (2004).
[5]M. H. Ettenberg, W. A. Jesser, and F. D. Rosi, presented at the Fifteenth International Conference on Thermoelectrics, (Pasadena, California, 1996).
[6]M. Carle, P. Pierrat, C. Lahalle-Gravier, S. Scherrer, and H. Scherrer, J. Phys. Chem. Solids **56**(2), 201 (1995).
[7]S. Scherrer and H. Scherrer, in *CRC Handbook of Thermoelectrics*, edited by D. Rowe (CRC, 1995), p. 211.
[8]X. Yan, B. Poudel, Y. Ma, W. S. Liu, G. Joshi, H. Wang, Y. Lan, D. Wang, G. Chen, and Z. F. Ren, Nano Lett. **10**(9), 3373 (2010).
[9]N. Peranio, O. Eibl, and J. Nurnus, J. Appl. Phys. **100**, 114306 (2006).
[10]N. Peranio and O. Eibl, J. Appl. Phys. **103**(2), 024314 (2008).
[11]H. J. Goldsmid, Proc. Phys. Soc. London, Sect. B **69**(2), 203 (1956).
[12]L. D. Hicks and M. S. Dresselhaus, Phys. Rev. B **47**(19), 12727 (1993).
[13]R. Venkatasubramanian, E. Siivola, T. Colpitts, and B. O'Quinn, Nature **413**(6856), 597 (2001).
[14]B. Poudel, Q. Hao, Y. Ma, Y. Lan, A. Minnich, B. Yu, X. Yan, D. Wang, A. Muto, D. Vashaee, X. Chen, J. Liu, M. S. Dresselhaus, G. Chen, and Z. Ren, Science **320**(5876), 634 (2008).
[15]N. Peranio and O. Eibl, Phys. Status Solidi A **204**(10), 3243 (2007).
[16]Z. C. Chen, K. Suzuki, S. Miura, K. Nishimura, and K. Ikeda, Mat. Sci. Eng. A **500**(1-2), 70 (2009).
[17]J. Seo, C. Lee, and K. Park, J. Mater. Sci. **35**(6), 1549 (2000).
[18]D. Maier, Solid State Commun. **122**(10), 565 (2002).
[19]A. Jacquot, T. Jürgen, J. Schumann, M. Jägle, H. Böttner, T. Gemming, J. Schmidt, and D. Ebling, J. Mater. Res. **26**, 1773 (2011).
[20]R. J. Mehta, Y. Zhang, C. Karthik, B. Singh, R. W. Siegel, T. Borca-Tasciuc, and G. Ramanath, Nature Mater. **11**(3), 233 (2012).
[21]N. Peranio and O. Eibl, Phys. Status Solidi A **206**(1), 42 (2009).
[22]K. Momma and F. Izumi, J. Appl. Cryst. **41**(3), 653 (2008).
[23]J. Bos, H. Zandbergen, M. H. Lee, N. Ong, and R. Cava, Phys. Rev. B **75**(19), 195203 (2007).
[24]D. L. Medlin, Q. M. Ramasse, C. D. Spataru, and N. Y. C. Yang, J. Appl. Phys. **108**(4), 043517 (2010).
[25]D. B. Williams and C. B. Carter, *Transmission Electron Microscopy: A Textbook for Materials Science*. (Plenum, 1996).
[26]A. Gomez-Rodriguez, L. M. Beltran-del-Rio, and R. Herrera-Becerra, Ultramicroscopy **110**, 95 (2010).
[27]N. Frangis, S. Kuypers, C. Manolikas, J. Van Landuyt, and S. Amelinckx, Solid State Commun. **69**(8), 817 (1989).
[28]C. L. Ciobanu, A. Pring, N. J. Cook, P. Self, D. Jefferson, G. I. Dima, and V. Melnikov, Am. Mineral. **94**(4), 517 (2009).
[29]F. Yu, J. Zhang, D. Yu, J. He, Z. Liu, B. Xu, and Y. Tian, J. Appl. Phys. **105**(9), 094303 (2009).
[30]W. Xie, X. Tang, Y. Yan, Q. Zhang, and T. M. Tritt, Appl. Phys. Lett. **94**(10), 102111 (2009).
[31]Z. Zhang, P. A. Sharma, E. J. Lavernia, and N. Yang, J. Mat. Res. **26**, 475 (2011).
[32]A. Kundu, N. Mingo, D. A. Broido, and D. A. Stewart, Phys. Rev. B **84**(12), 125426 (2011).
[33]See supplementary material at http://dx.doi.org/10.1063/1.4759285 for x-ray diffraction data, TEM images showing porosity, phonon scattering schematics, and single crystal TEM investigation.